Computer Methods in Biomechanics and Biomedical Engineering, 2002 Vol. 5 (4), pp. 309–318

Taylor & Francis
Taylor & Francis Group

Flow-induced Wall Shear Stress in Abdominal Aortic Aneurysms: Part I – Steady Flow Hemodynamics

ENDER A. FINOL* and CRISTINA H. AMON

Mechanical Engineering, Biomedical and Health Engineering, and Institute for Complex Engineered Systems, Carnegie Mellon University, Pittsburgh, PA

(Received 18 September 2000; In final form 6 March 2001)

Numerical predictions of blood flow patterns and hemodynamic stresses in Abdominal Aortic Aneurysms (AAAs) are performed in a two-aneurysm, axisymmetric, rigid wall model using the spectral element method. Homogeneous, Newtonian blood flow is simulated under steady conditions for the range of Reynolds numbers $10 \leq \mathrm{Re} \leq 2265$. Flow hemodynamics are quantified by calculating the distributions of wall pressure (p_w), wall shear stress (τ_w), Wall Shear Stress Gradient (WSSG). A correlation between maximum values of hemodynamic stresses and Reynolds number is established, and the spatial distribution of WSSG is considered as a hemodynamic force that may cause damage to the arterial wall at an intermediate stage of AAA growth. The temporal distribution of hemodynamic stresses in pulsatile flow and their physical implications in AAA rupture are discussed in Part II of this paper.

Keywords: Hemodynamics; Aneurysms; Steady flow; Shear stress; Wall shear stress gradient

INTRODUCTION

Abdominal Aortic Aneurysms (AAAs) are irreversible dilations due to a weakening of the wall of the aorta in its abdominal segment; they are present when there is an increase in the diameter greater than 50% the diameter of the normal adjacent arterial portion. Statistics show that abdominal aortic aneurysm rupture affects 1 in 250 individuals greater than 50 years of age and males are affected more often than women in a ratio of 4:1. As the 5-year survival rate is only 19% and the overall mortality rate following aneurysm rupture may exceed 90% [1], determining the risk factors that may have an important role in aneurysm growth and rupture has become an integrated multidisciplinary task oriented towards obtaining a thorough understanding on the pathogenesis and evolution of AAAs. It is well known now that arterial diseases, present in local irregular geometries, are the result of a combination of biochemical processes that take place in the vascular wall at the cellular level as well as the hemodynamics resulting from the interaction of blood flow and the inner wall. It is the purpose of this work to provide new insights into indicators that have been recently proposed for the quantification of blood flow hemodynamics, under steady and pulsatile conditions, through abdominal aortic aneurysm models.

Several experimental and numerical studies of blood flow at constant flow rates through aneurysms are found in the literature. Flow visualization studies for steady flow in *in-vitro* spherical models of aneurysms resulted in the determination of streamline patterns inside the bulge models [2]. These results show the formation of a jet of fluid passing through the aneurysm, surrounded by a region of recirculating flow. Stehbens [3] observed boundary layer separation and reattachment in flow visualization experiments with glass models of different aneurysm shapes and sizes. Quantitative flow measurements in fusiform and saccular glass models of aortic aneurysms were performed by Musto and Roach [4]. Drexler and Hoffmann [5] made improvements in experimental modeling and observed regions of stagnant and reversed flow in asymmetric casting resin models of aneurysms. Numerical and experimental studies of steady flow performed by Budwig *et al.* [6] demonstrate the effect of flow patterns in the distribution of pressure and shear stresses at the wall. The steady flow numerical simulations of Taylor and Yamaguchi [7] show the existence of two symmetric vortices in three-dimensional asymmetric computational models. Peattie and colleagues [8–10] observed that wall pressure inside the aneurysm model reaches a maximum at the centre, while turbulence increases wall shear stresses by an order of magnitude at

*Corresponding author. Tel. (412) 268-2497/2491/2511/3689, Fax: (412) 268-3348.

ISSN 1025-5842 print/ISSN 1476-8259 online © 2002 Taylor & Francis Ltd
DOI: 10.1080/1025584021000009742

the distal edge of the bulge. Correlation between steady blood flow dynamics and rates of platelet deposition proved the existence of a monotonic increase of platelet aggregation at the aneurysm wall, until reaching a maximum at the distal edge [11,12].

In this paper, flow patterns and their effect on wall shear stress levels and wall pressure distributions are revisited for a two-aneurysm model. Wall Shear Stress Gradients (WSSGs) in the normal and tangential directions to the wall are also evaluated. Additionally, a correlation between maximum values of the hemodynamic stresses and the Reynolds number is developed. In Part II of this investigation, numerical predictions of the oscillatory effect of wall pressure, wall shear stresses, WSSGs, and other hemodynamic indicators are presented for pulsatile flow at different time-average flow rates.

GOVERNING EQUATIONS

The geometry of the abdominal aorta with two aneurysms is shown in Figure 1. Two wavy-walled regions define this geometry, the physical model of which has been used previously by Finol and Amon [13,14], and Guzmán *et al.* [15,16]. We consider incompressible, homogeneous, Newtonian flow in a two-aneurysm rigid axisymmetric model with sinusoidal walls. Although blood is actually a non-Newtonian suspension of cells in plasma, it is reasonable to model it as a Newtonian fluid in vessels greater than approximately 0.5 mm in diameter [17]. The deformed wall is represented by two sine functions as follows:

$$f(z) = \begin{cases} \left(\frac{D_1 - D}{4}\right)\left[1 + \sin\left(\frac{2\pi z}{L_1} - \frac{\pi}{2}\right)\right] + \frac{D}{2} \\ 0 \le z \le L_1 \end{cases} \quad (1a)$$

$$\begin{cases} \left(\frac{D_2 - D}{4}\right)\left[1 + \sin\left(\frac{2\pi (z - L_1)}{L_2} - \frac{\pi}{2}\right)\right] + \frac{D}{2} \\ L_1 \le z \le L_1 + L_2 \end{cases} \quad (1b)$$

The momentum and continuity equations in axisymmetric coordinates that govern unsteady, incompressible and Newtonian flows are given by

$$\rho\left(\frac{\partial u_z}{\partial t} + \vec{\mathbf{V}}\cdot\nabla u_z\right) = -\frac{\partial p}{\partial z} + \left(\frac{\partial \tau_{zz}}{\partial z} + \frac{1}{r}\frac{\partial}{\partial r}(r\tau_{rz})\right) \quad (2a)$$

$$\rho\left(\frac{\partial u_r}{\partial t} + \vec{\mathbf{V}}\cdot\nabla u_r\right) = -\frac{\partial p}{\partial r} + \left(\frac{\partial \tau_{rz}}{\partial z} + \frac{1}{r}\frac{\partial}{\partial r}(r\tau_{rr})\right) \quad (2b)$$

$$\frac{1}{r}\frac{\partial}{\partial r}(ru_r) + \frac{\partial u_z}{\partial z} = 0 \quad (2c)$$

where $\vec{\mathbf{V}}(\vec{r}, t) = u_r\hat{r} + u_z\hat{z}$ is the velocity vector, and τ_{zz}, τ_{rr} and τ_{rz} are the components of the two-dimensional stress tensor. The stress components are determined using the Newtonian flow constitutive relationship, as given by Eq. (3), since incompressible flows satisfy the divergence-free condition for the velocity ($\nabla\cdot\vec{\mathbf{V}}$) :

$$\tau_{ij} = -p\delta_{ij} + \mu\left(\frac{\partial u_i}{\partial x_j} + \frac{\partial u_j}{\partial x_i}\right) \quad (3)$$

Boundary conditions for the velocity $\vec{\mathbf{V}}(\vec{r}, t)$ are imposed as follows: (i) no slip at the walls, (ii) symmetry at the centreline, (iii) fully developed parabolic profile at the inlet, and (iv) zero-traction outflow condition at the exit. An outflow length has been added to account for the zero-traction outflow condition, which is equivalent to half the length of the dilated portion of the artery, or 3.75 inlet diameters. Average blood properties [18] are used for constant blood flow simulation: molecular viscosity $\mu = 0.00319$ Pa·s and density $\rho = 1.050\,\mathrm{kg/m^3}$. The governing equations are nondimensionalized by the factor D; hemodynamic indicators evaluated at the arterial wall are nondimensionalized using their corresponding magnitudes obtained for Poiseuille flow.

The calculation of the local Wall Shear Stress Gradient (WSSG) is based on the predictor equation proposed by Lei and Kleinstreuer [19] at the cellular level:

$$\mathrm{WSSG} = \sqrt{\left(\frac{\partial \tau_w}{\partial \hat{t}}\right)^2 + \left(\frac{\partial \tau_w}{\partial \hat{n}}\right)^2} \quad (4)$$

where $\hat{t}$ and $\hat{n}$ are the local tangential and normal directions to the wall, as shown in Figure 1. The calculation of the terms within the WSSG indicator follows a different procedure than that implied in the statement of Lei's zero-tension hypothesis. It is not our intention to compare values of WSSG at the cellular level to those that would be expected at the wall of an abdominal aneurysm. Moreover, the presence of an AAA indicates a severely eroded intima (absence of endothelium).

METHODOLOGY

The governing equations, subject to the appropriate boundary conditions, are solved numerically using the Spectral Element Method (SEM) for the spatial discretization. The computational domain, shown in Figure 2, is composed of 228 quadrilateral macro-elements, with 76 in the axial direction. Mesh resolution tests have been conducted with the geometry using 304 macroelements (4 macroelements in the cross-streamwise direction). The numerical results did not reveal any significant changes when compared to the 228-macroelement mesh used to report the results of our work. The geometry and variables are isoparametrically mapped by using fifth-order polynomial expansions in each direction per macro-element. Thus, each macro-element is subdivided into a nonuniform local Cartesian grid that corresponds to 5×5 Gauss–Lobatto–Chebyshev collocation points. These

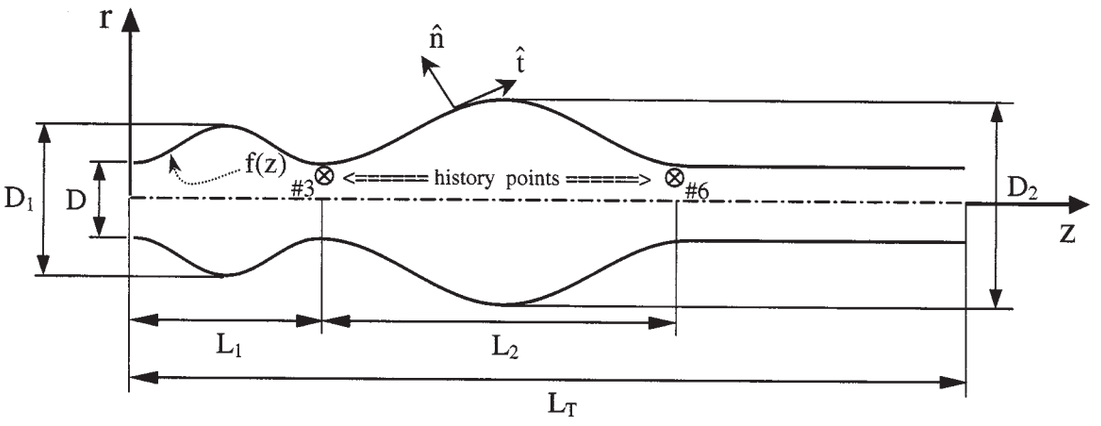

FIGURE 1 Representation of the axisymmetric model of the abdominal aorta with a double-aneurysm, for which $L_1 = 2.5\,D$, $L_2 = 5D$, $LT = 11.25D$, $D_1 = 2D$, and $D_2 = 2.75D$.

points are clustered near the boundaries of the macro-elements, and the transport variables evaluated at each point are expressed in terms of tensor products of high-order Lagrangian interpolants. A three-step time-splitting scheme is used for the semidiscrete formulation of the time-dependent terms in the momentum equations. The Spectral Element Method has been widely used for the Direct Numerical Simulation (DNS) of transitional flows with fast evolving temporal phenomenon and complex geometries. For more information on validation studies performed with SEM and a detailed description of the numerical method, the reader is referred to Patera [20], and Amon [21,22].

RESULTS AND DISCUSSION

Numerical results are obtained at Reynolds numbers over the range $10 \leq Re \leq 2265$. The Reynolds number is based on the undilated artery diameter (diameter of the model at $z = 0$, Fig. 1) and the average velocity at the entrance of the artery. In the constant flow simulations, the inlet velocity profile is parabolic, corresponding to a fixed inlet flow rate. A time-dependent initial value code is used to find the asymptotic solution to steady flow, starting from arbitrary initial conditions. The pressure at the exit of the double-aneurysm model is set to 0 Pa; therefore, all the pressure results are relative to this value.

Flow Patterns

Figure 3 shows typical laminar flow streamlines for the range of Reynolds number $10 \leq Re \leq 2265$. At $Re = 10$, corresponding to a blood flow rate of $1.91 \times 10^{-7}\,m^3/s$ (0.012 L/min), no flow separation occurs, and the main stream of fluid fills completely each of the arterial dilatations in a forward flow pattern. The converging–diverging shape of the model produces successive convective decelerations and accelerations of the flow that result in very small axial velocities near the wall at the centre of each aneurysm. The onset of flow separation is found to occur within the range $24.7 < Re < 25$. For $Re = 25$, negative axial velocities in the order of magnitude of $10^{-7}\,m/s$ are obtained close to the wall.

A characteristic flow pattern is shown in Figures 3(b) through 3(f): an inner core flow that passes through each dilatation and two main surrounding regions of flow recirculation and separation. This laminar flow field agrees with the flow visualization experiments conducted by Asbury [8]. The symmetrically recirculating regions inside the arterial expansions are characterized by an upper subregion of reversed flow, which interacts with the aneurysm wall, and a lower subregion of forward flow that

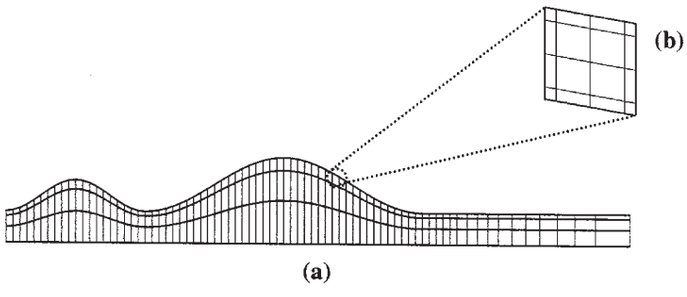

FIGURE 2 Axisymmetric double-aneurysm spectral element mesh: (a) macro-element discretization, and (b) local element decomposition.

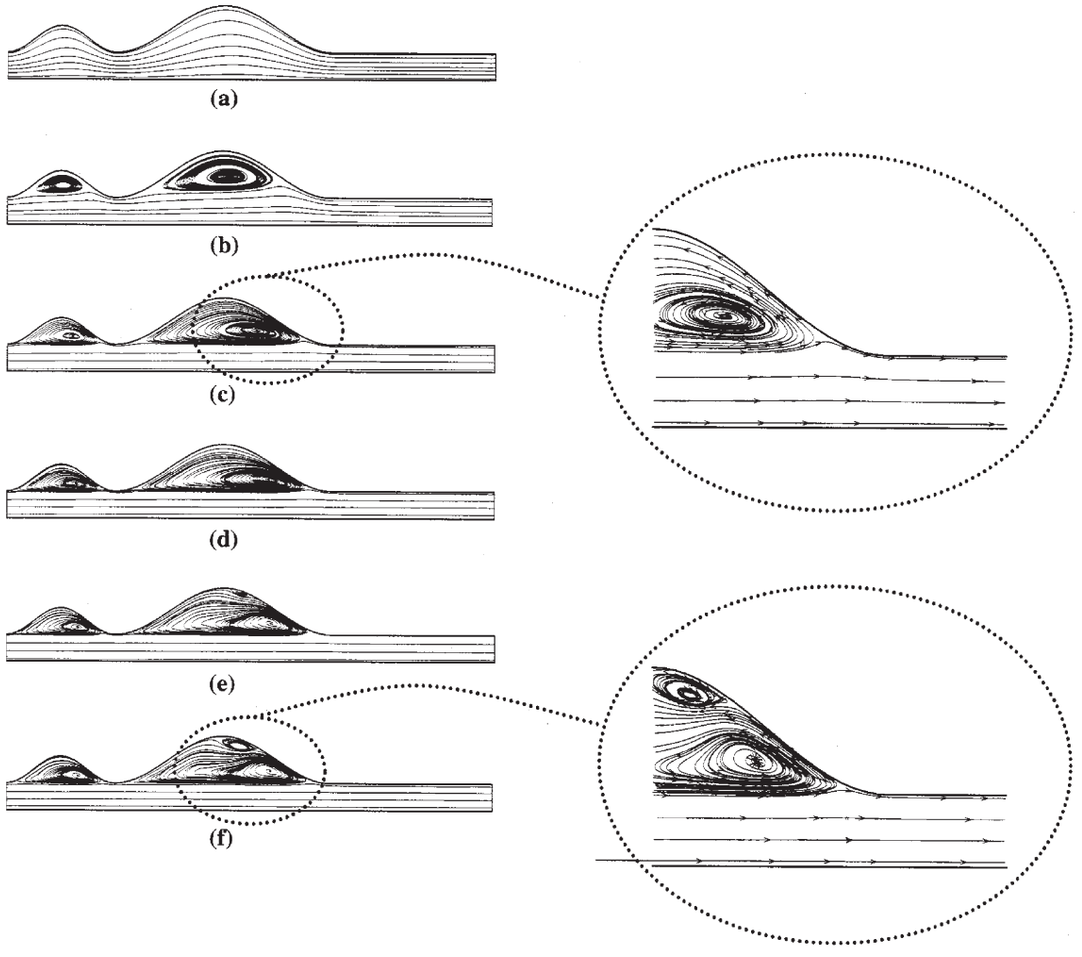

FIGURE 3 Streamlines for laminar steady flow at (a) Re = 10, (b) Re = 100, (c) Re = 500, (d) Re = 1000, (e) Re = 1750, and (f) Re = 2265. The direction of the flow is from left to right.

is sheared by the fluid core. For $Re \geq 500$, the fluid moving in reverse direction occupies most of the aneurysm sac volume, while the forward moving fluid in the vortex fills in a very small portion of the expansion. This is represented by a contraction of the streamlines in the distal half of each aneurysm, to the right and below the centre of the vortex, and an expansion of the streamlines in the proximal half, especially close to the wall. Consequently, the upper subregion is essentially a zone of slowly moving particles of fluid, nearly stagnant, of high distal and low proximal shear due to blood flow-wall interaction. At each aneurysm enlargement, streamline separation occurs upstream. The dividing streamline represents particles of fluid that, after separation, continue flowing downstream, along the undisturbed moving core. Particles traveling above the dividing streamline are trapped within the aneurysm sac, and upon reaching the distally located boundary layer reattachment region, reverse their direction, flowing backwards along the wall, towards the separation point. Therefore, fluid along the wall moves in accord with the local pressure gradient and after traveling the longitudinal perimeter of the aneurysm, the core flow, which is faster, separates from the wall and forms a laminar main stream with an annular region of flow recirculation.

As the Reynolds number is increased, the centre of the recirculating flow regions moves downstream and also downward, closer to the main stream. This causes the displacement of the boundary layer separation points further upstream, and the reattachment points further downstream, increasing the volume occupied by the vortices within the aneurysm sacs. In the range $500 < Re \leq 2265$, however, the movement of the vortex center occurs towards the distal end of each aneurysm, but not closer to the main stream. This results in a fairly constant core flow volume through the model for the higher flow rates [$9.54 \times 10^{-6}\,m^3/s$ (0.57 L/min) $< Q \leq 4.32 \times 10^{-5}\,m^3/s$ (2.59 L/min)], which agrees qualitatively with the experimental observations of Scherer [2] and his comparison with inviscid theory. Our numerical results predict flow unsteadiness for $Re \geq 1750$, which is observed in history plots of axial velocity and pressure. For this range of Reynolds numbers, an induced secondary vortex is formed in the large

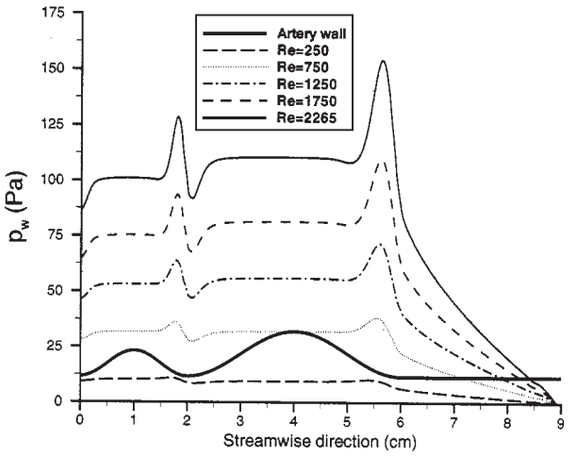

FIGURE 4 Pressure distribution along the wall of the double-aneurysm model for selected Reynolds numbers.

aneurysm. This small vortex, which increases in size and intensity for Re = 2265, is clockwise-rotating, indicating the presence of positive wall velocity gradients. The formation of a second recirculation region, trapped between the aneurysm wall and the main vortex, occurs for a range of Reynolds numbers for which unsteadiness and transition to turbulence has also been observed experimentally [6,8–10]. Therefore, an intermittent transitional flow regime characterizes the results obtained for $1750 \leq Re \leq 2265$.

Wall Pressure

Figure 4 shows the wall pressure distribution throughout the two-aneurysm model, relative to the exit pressure of 0 Pa. The relatively small pressure gradient generated at Re = 250 results in a distribution of pressure at the wall that cannot be seen clearly for the vertical axis scale chosen in this figure. The total pressure drop for this case is only 9.3 Pa. For $750 \leq Re \leq 2265$, the recirculating flow and the change in cross-sectional area upstream of the small aneurysm induces an increase in the wall pressure in the vicinity of the boundary layer separation point. The pressure then reaches a plateau, remaining fairly constant through the aneurysm until the point of flow reattachment. At this point, essentially a stagnation point, the wall pressure peaks and then decreases abruptly at the distal end of the aneurysm. The site of minimum wall pressure for the small aneurysm is obtained at z = 2 cm, where the cross-sectional area is that of the undilated artery. The convective acceleration of the flow after boundary layer reattachment, due to the converging shape downstream of the aneurysm, is not enough to produce the pressure drop that would be expected at z = 2 cm for a healthy, non-aneurysmal artery. Therefore, the fluid enters the large aneurysm having a higher arterial wall pressure and then drops down to 0 Pa at the exit. Consequently, the wall pressure gradient in the large aneurysm is greater than in the small aneurysm. The wall pressure variation along the large aneurysm is qualitatively similar to the one along the small aneurysm; the pressure remains constant along the aneurysm and then peaks at the flow reattachment point. Iso-pressure contours, shown in Figure 5 for Re = 1500, demonstrate that the pressure remains constant along most of the dilated wall, reaching a maximum at the points of flow reattachment. At these points there is a concentration of the isobars before the pressure falls sharply downstream of each aneurysm.

Two observations can be made regarding Figure 4. First, the Bernoulli-type of wall pressure variation reported by [8–10], in which the maximum pressure occurs at the midpoint of the aneurysm is not obtained in viscous flow. This can be explained by the fact that in the recirculation region, the fluid moving along the aneurysm wall travels in reverse direction, along the local pressure gradient, while the faster moving fluid core separates from the wall and travels undisturbed through the aneurysm. In the aneurysms, the wall shears the low-momentum fluid and, thus, viscous forces are significant in order to balance the pressure gradient and the convective deceleration of the flow along most of the aneurysm wall. As the Reynolds number increases, larger velocity gradients occur in the recirculation region, helping to maintain a region of almost constant wall pressure. Second, the nearly constant pressure along the aneurysm wall is a result obtained truly for the higher Reynolds numbers, $500 \leq Re \leq 2265$. For $Re \leq 250$ there is a very small monotonic increase of the wall pressure along each aneurysm before reaching a local maximum at the reattachment point.

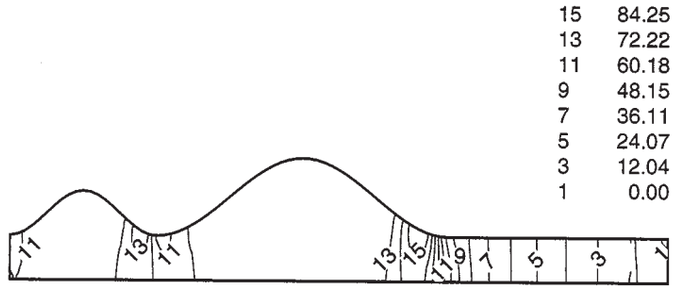

FIGURE 5 Isobars (pressure contours) for Re = 1500; ten isobars are specified in Pascal.

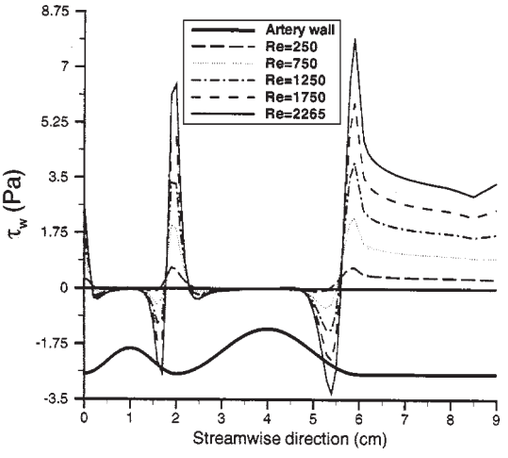

FIGURE 6 Wall shear stress distribution for selected Reynolds numbers.

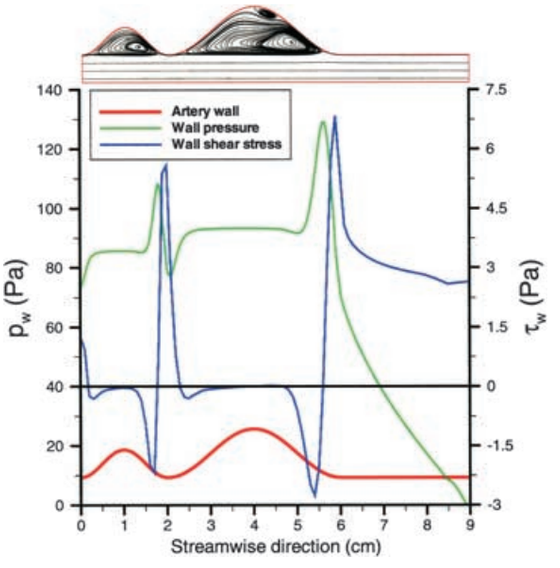

FIGURE 7 Wall pressure, wall shear stress, and streamlines for Re = 2000.

Wall Shear Stress

The shear stress distribution at the arterial wall is shown in Figure 6. The inlet wall shear stress is equal to that of Poiseuille flow, for which the artery is undilated. The convective deceleration of the flow in the proximal half of the small aneurysm induces very small velocity gradients at the wall, which results in a decrease in the wall shear stress to a near zero magnitude. For $\mathrm{Re} \geq 250$, the negative velocity gradients within the small aneurysm wall cause a low negative wall shear stress at the center of the aneurysm, which is no more than 3% of the inlet wall shear stress. The point at which the wall shear stress changes sign in the proximal end is the site of boundary layer separation (a stagnation point); this occurs at $z = 0.24$ cm for $\mathrm{Re} = 250$, and at $z = 0.16$ cm for $\mathrm{Re} = 2265$. Similarly, the zero shear stress value in the distal end is the site of boundary layer reattachment; this occurs at $z = 1.56$ cm for $\mathrm{Re} = 250$, and at $z = 1.78$ cm for $\mathrm{Re} = 2265$. The vicinity of the reattachment point is a site of localized low negative and high positive wall shear stress, with the minima and maxima occurring at about the same location for every case within the $250 \leq \mathrm{Re} \leq 2265$ range. The low negative shear stress occurs at $z = 1.65$ cm, which is the point of maximum contraction of the streamlines within the recirculation region. Therefore, larger velocity gradients are obtained, compared to those at the centre of the small aneurysm. The high positive shear stress occurs at $z = 1.92$ cm, very close to the location of the minimal cross-sectional area, due to the development of a new boundary layer. The flow then enters the large aneurysm and the same pattern of zero wall shear stress at the separation/reattachment points and local low/high shear stresses in the distal end is repeated. The magnitude of the wall stresses is greater in the large aneurysm at the same Reynolds number. At the centre of the aneurysm, however, the negative wall shear stress is much lower, an almost zero magnitude. The sharp drop seen in the distal area of the large aneurysm upon reaching the maximum value corresponds to the straightening of the streamlines at the exit of the aneurysm into the straight arterial wall.

The discussion based on Figures 4 and 6 demonstrates that the distal end of each aneurysm is a region where viscous interaction of blood flow and the tunica intima yields high and low shear stresses at the wall and high wall pressure within a recirculation zone where boundary layer reattachment occurs. Muraki [23] observed that this region is the most likely site of aneurysm rupture. In order to visualize this interaction of wall shear stresses and wall pressure, a superposition of the p_w and τ_w curves is presented for $\mathrm{Re} = 2000$ in Figure 7.

Wall Shear Stress Gradient

Distributions of high and low wall shear stresses within a localized region in the artery wall indicate the existence of high levels of Wall Shear Stress Gradients (WSSGs). The WSSG indicator defined in Eq. (4) and shown in Figure 8 for different Reynolds numbers quantifies the variation of shear stress in the normal and tangential direction to the wall. The WSSG at the entrance of the small aneurysm is due to the change in wall shear stress at $z = 0$ (*i.e.*, for Poiseuille flow) to the negative shear stress obtained at the point of flow separation upstream of the small aneurysm. For $\mathrm{Re} = 250$, the low negative shear stress obtained after the flow separates has an almost constant value until reaching the distal end, and thus a zero mean WSSG is obtained for $0.41\,\mathrm{cm} < z < 1.69\,\mathrm{cm}$. For $\mathrm{Re} = 2265$, this range of nearly constant wall shear stress is reduced to $0.50\,\mathrm{cm} < z < 1.19\,\mathrm{cm}$, which suggests that a greater variation of velocity gradients occurs at both ends of the small aneurysm as the Reynolds number increases.

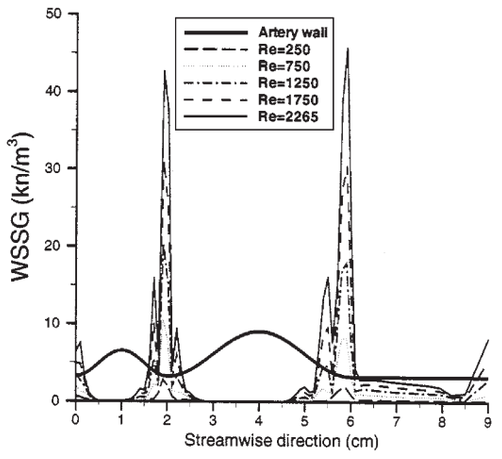

FIGURE 8 Distribution of shear stress gradient along the wall for selected Reynolds numbers.

The highest values of WSSGs are obtained at the sites of flow reattachment. The change of sign of the shear stress at these locations results in the first peak of the WSSG curves downstream of the small aneurysm, and the second peak downstream of the large aneurysm. Between the two points there is a decrease in the WSSG value corresponding to another change of sign of shear stress, characteristic of flow reattachment.

The pattern for WSSG distribution is very similar for the large aneurysm: flow separation occurs upstream resulting in a non-zero WSSG at the entrance of the aneurysm. This value is greater than the WSSG at the entrance of the small aneurysm because of the larger upstream negative velocity gradient in the large aneurysm. The extension of the zero WSSG region is greater for the large aneurysm; for $Re = 250$ it is given by $2.53\,cm < z < 5.19\,cm$, and for $Re = 2265$ by $2.82\,cm < z < 4.59\,cm$. The increase in aneurysm diameter and length results in higher levels of WSSG at the site of flow reattachment; for $Re = 2265$ a $WSSG_{max}$ of $45.9\,kN/m^3$ is obtained for the large aneurysm, compared to $42.7\,kN/m^3$ for the small aneurysm. No experimental measurements of WSSGs in aneurysms have been reported previously in the literature.

Correlation Functions

The correlation of wall hemodynamics with the Reynolds number is established by means of a fourth order polynomial function of the form:

$$\Phi_w = \sum_{i=0}^{4} a_i Re^i \tag{5}$$

where $\Phi_w = f(Re)$ is any hemodynamic indicator evaluated at the wall (*e.g.*, τ_w, WSSG, or p_w). Table I shows the coefficients resulting from this correlation in the appropriate units, and Figure 9 shows the polynomial curves and the discrete minimum and maximum values of the hemodynamic indicators as a function of the Reynolds number.

The minimum (negative) and maximum (positive) wall shear stress, obtained in the distal end of the small and large aneurysm is shown in Figure 9(a). A monotonic increase of the maximum values is observed for both aneurysms as the Reynolds number increases, while the minimum shear stress decreases with Re. The effect of increasing aneurysm size results in higher levels of shear stress and WSSG; the maximum WSSG curve for the large aneurysm (shown in Figure 9(b)) has a significant slope increase for $Re \geq 1850$. This can be explained by the fact that for $Re \geq 1850$ the point of flow reattachment in the large aneurysm has moved downstream closer to the exit, and thus the coexistence of high and low levels of shear stress occurs within less than 0.4 cm of the outflow section. This induces larger velocity gradients in the distal end, higher maximum shear stresses higher WSSGs. A similar explanation is valid for and describing the wall pressure distribution as a function of the Reynolds number, shown in Fig. 9(c): an increase in aneurysm length and diameter is translated into more axial length available for displacement of the boundary layer reattachment point in the direction of the flow, as the Reynolds number is increased.

CONCLUSIONS

Spectral element numerical simulations of constant, incompressible, homogeneous, Newtonian blood flow in

TABLE I Correlation coefficients for maximum and minimum wall shear stress, maximum wall shear stress gradient, and maximum wall pressure as a function of the Reynolds number, according to Eq. (5)

		Correlation coefficients				
Hemodynamic indicator		$a_4 \times 10^{14}$	$a_3 \times 10^{10}$	$a_2 \times 10^{6}$	$a_1 \times 10^{3}$	$a_0 \times 10^{2}$
($\tau_{w,min}$	Small AAA	−10.57	5.177	−1.099	−0.119	0.652
	Large AAA	−5.579	3.617	−1.120	−0.136	1.024
$\tau_{w,max}$	Small AAA	0.554	−0.288	0.083	2.605	−0.655
	Large AAA	6.242	−3.535	0.940	2.464	−1.633
$WSSG_{max}$	Small AAA	31.13	−24.04	7.983	9.503	−3.095
	Large AAA	8.678	−9.680	8.369	5.272	−3.303
$p_{w,max}$	Small AAA	296.4	−127.6	22.11	37.70	−0.723
	Large AAA	312.6	−153.3	34.32	32.62	−6.984

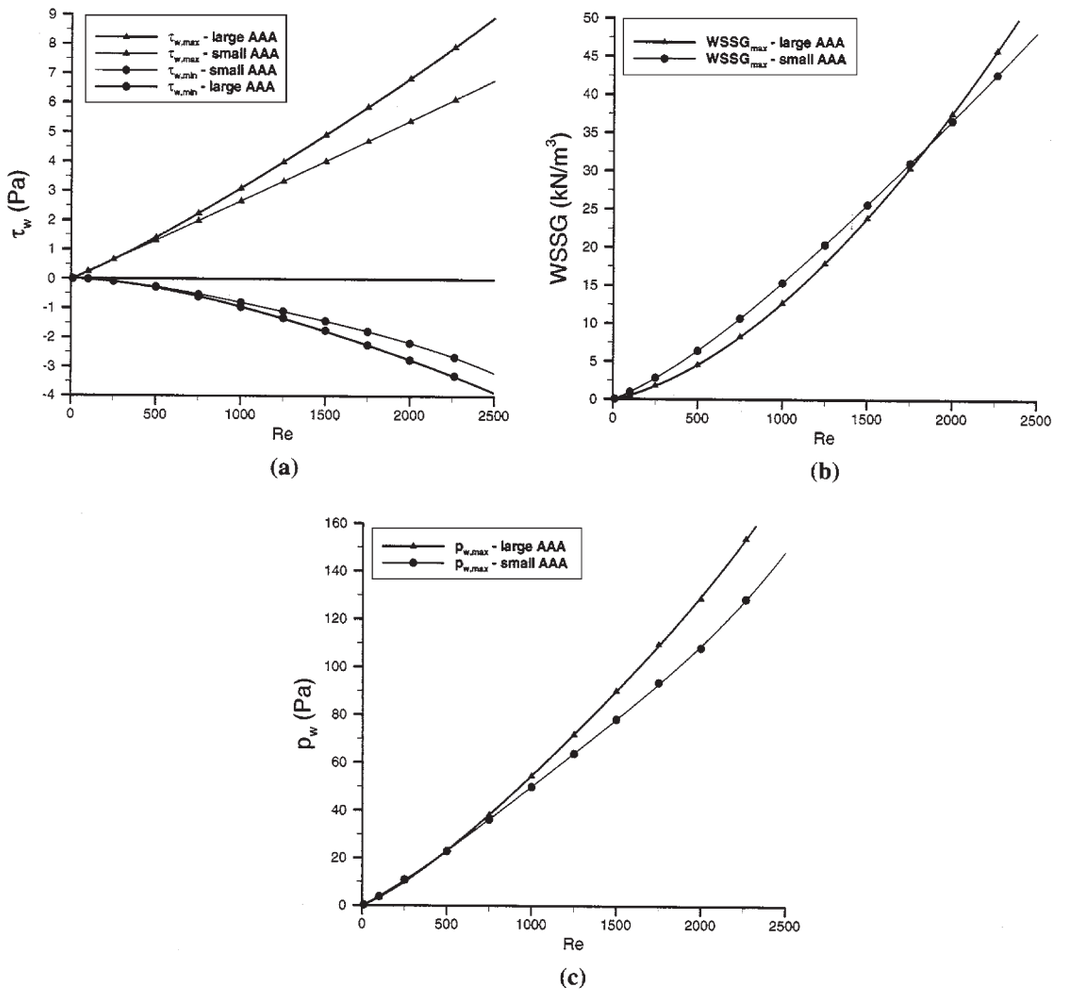

FIGURE 9 Dependence of wall hemodynamics on Reynolds number for small and large aneurysms: (a) maximum and minimum wall shear stress; (b) maximum wall shear stress gradient; (c) maximum wall pressure.

a double-aneurysm rigid model have been presented. The numerical results describe the vortex structure of the flow in each aneurysm and its relationship to the magnitude and spatial distribution of relevant hemodynamic indicators.

It has been shown that the fluid dynamics characterizing non-pulsatile blood flow in AAAs is represented by a single region of slowly recirculating fluid inside each aneurysmal expansion, in the laminar regime. As the Reynolds number is increased, the vortex evolution influences the distribution of the hemodynamic indicators. Flow unsteadiness is observed for $1750 \leq \mathrm{Re} \leq 2265$, a range of Reynolds numbers for which previous experimental studies have proven the existence of transition to turbulence. In the transitional flow regime, our numerical results indicate that a second recirculation region is induced by the main vortex and trapped against the wall, near the centre of the large aneurysm. Convective acceleration and deceleration of the flow, and viscous interaction between the wall and the fluid, determine wall pressure patterns, which are particularly significant at the sites of boundary layer reattachment. These sites occur in the distal end of each aneurysm and are characterized by a high wall pressure, which is greater in the large aneurysm. High (positive) and low (negative) wall shear stresses are obtained in the vicinity of the flow reattachment, while a low and almost constant shear stress is typical at the centre of both aneurysms. Therefore, a highly disturbed flow is seen downstream of each aneurysm, proven by previous studies to be the region where an aneurysm would most likely rupture.

The hemodynamics in aneurysms, quantified by the Wall Shear Stress Gradient (WSSG), indicates the spatial variation of shear stresses in the normal and tangential direction to the wall. High WSSGs are obtained at the sites of sign change of the wall shear stress, further supporting the evidence that the distal end of the aneurysm is the region where significant hemodynamic disturbance takes place. Maximum values of WSSG, which increase with the Reynolds number and aneurysm size, are obtained downstream of the sites of flow reattachment. These values may be up to an order of magnitude greater than those expected for a normal, healthy aorta under the same

mean flow conditions. The centre of each aneurysm is exposed to a nearly zero WSSG. due to almost no change in the velocity gradients at these locations. In addition, the monotonic nonlinear increase of the maximum wall pressure, wall shear stress and WSSG with the Reynolds number is correlated by a fourth order polynomial function.

The rigid wall assumption is an important limitation to the present study. The objective of conducting flow calculations using rigid wall, two-dimensional axisymmetric models is to obtain an initial understanding of the flow physics within an artery model with converging-diverging walls. To provide an assessment for AAA growth and rupture, there is need to couple flow hemodynamics with wall mechanics. Further investigation is currently being conducted by developing three-dimensional wall-compliant asymmetric computational models based on patients' digitized Magnetic Resonance images of AAAs. These models are used for numerical simulations of steady and pulsatile flow with wall interaction to compute the inner wall stresses induced by the flow. Despite the rigid wall assumption and the limitation of axisymmetry, the present study provides insight into the location and estimation of wall shear stress within a bulge or arterial expansion, which can prove to be valuable for the calculation of flow-induced stresses in a 3-D distensible wall model. The results presented in this manuscript serve as initial predictions for the expected results of the large-scale simulations employing 3-D aneurysm models with a varying degree of asymmetry.

Acknowledgements

The authors gratefully acknowledge the support of the National Science Foundation grant CTS-9630801, the Whitaker Foundation grant RG-96-0202, and the Pennsylvania Infrastructure Technology Alliance Partnership from the Commonwealth of Pennsylvania's Department of Economic and Community Development.

NOMENCLATURE

The following is a list of symbols and abbreviations used in Parts I and II of this paper:

AAA	Abdominal Aortic Aneurysm
D	Inlet diameter of two-aneurysm model
D_1	Maximum diameter of small aneurysm, $D_1 = 2D$
D_2	Maximum diameter of large aneurysm, $D_2 = 2.75D$
L_1	Length of small aneurysm, $L_1 = 2.5D$
L_2	Length of large aneurysm, $L_2 = 5D$
p	Blood pressure
$\bar{Q}$	Time–average volumetric flow rate, $\bar{Q} = \pi(D^2/4)\bar{u}_m$
r	Radial coordinate measured from the model symmetry axis
Re	Reynolds number, $Re = D\bar{u}/v$
Re_m	Time–average Reynolds number
Re_{peak}	Instantaneous Reynolds number at peak flow ($t = 0.31$ s)
t	Time
$\hat{t}$, $\hat{n}$	Local tangential and normal directions to the wall
T_p	Time period of pulsatile cycle
$\bar{u}_m$	Time–average inflow mean velocity
$\vec{V}$	Velocity vector
WSSG	WallShearStressGradient
WSSG*	Instantaneous nondimensional Wall Shear Stress Gradient
$\overline{WSSG}^*$	Time–average nondimensional Wall Shear Stress Gradient
z	Longitudinal coordinate measured from the inlet
α	Womersley number, $\alpha = (D/2)\sqrt{\omega/v}$
γ	Amplitude coefficient of pulsatile flow, $\gamma = Re_{peak}/Re_m$
μ	Molecular viscosity of blood
ν	Kinematic viscosity of blood, $\nu = \mu/\rho$
ω	Frequency of pulsatile flow, $\omega = 2\pi/T_p$
ρ	Blood density
τ	Fluid shear stress
τ_w^*	Instantaneous nondimensional wall shear stress
$\overline{\tau_w}^*$	Time–average nondimensional wall shear stress
τ_{wo}	Wall shear stress for Poiseuille flow evaluated at Re_m

Subscript

w	Indicates a parameter evaluated at the wall

Superscript

*	Indicates a nondimensional parameter

References

[1] Ernst, C. (1993) "Abdominal Aortic Aneurysm", *The New England Journal of Medicine* **328**, 1167–1172.

[2] Scherer, P. (1973) "Flow in Axisymmetrical Glass Model Aneurysms", *Journal of Biomechanics* **6**, 695–700.

[3] Stehbens, W. (1974) "Flow Disturbances in Glass Models of Aneurysms at low Reynolds Numbers", *Quarterly Journal of Experimental Physiology* **59**, 167–174.

[4] Musto, R. and Roach, M. (1980) "Flow Studies in Glass Models of Aortic Aneurysms", *The Canadian Journal of Surgery* **23**, 452–455.

[5] Drexler, D. and Hoffman, A. (1985) "Steady Flow through several Aneurysm Models", In: Kuklinski, W. and Ohley, W., eds, Proceedings from the 11th Annual Northeast Bioengineering Conference, pp 147–150.

[6] Budwig, R., Elger, D., Hooper, H. and Slippy, J. (1993) "Steady flow in Abdominal Aortic Aneurysm Models", *ASME Journal of Biomechanical Engineering* **115**, 418–423.

[7] Taylor, T. and Yamaguchi, T. (1994) "Three-Dimensional Simulation of Blood Flow in an Abdominal Aortic Aneurysm—Steady and Unsteady Flow Cases", *ASME Journal of Biomechanical Engineering* **116**, 89–97.

[8] Asbury, C., Ruberti, J., Bluth, E. and Peattie, R. (1995) "Experimental Investigation of Steady Flow in Rigid Models of Abdominal Aortic Aneurysms", *Annals of Biomedical Engineering* **23**, 29–39.

[9] Peattie, R., Bluth, E., Ruberti, J. and Asbury, C. (1996) "Steady Flow in Models of Abdominal Aortic Aneurysms—Part I:

Investigation of Velocity Patterns", *Journal of Ultrasound in Medicine* **15**, 679–688.

[10] Peattie, R., Bluth, E., Ruberti, J. and Asbury, C. (1996) "Steady Flow in Models of Abdominal Aortic Aneurysms—Part II: Wall Stresses and Their Implication for In Vivo Thrombosis and Rupture", *Journal of Ultrasound in Medicine* **15**, 689–696.

[11] Schoephoerster, R., Oynes, F., Nunez, G., Kapadvanjwala, M. and Dewanjee, M. (1993) "Effects of Local Geometry and Fluid Dynamics on Regional Platelet Deposition on Artificial Surfaces", *Arteriosclerosis and Thrombosis* **13**, 1806–1813.

[12] Bluestein, D., Niu, L., Schoephoerster, R. and Dewanjee, M. (1996) "Steady Flow in an Aneurysm Model: Correlation between Fluid Dynamics and Blood Platelet Deposition", *ASME Journal of Biomechanical Engineering* **118**, 280–286.

[13] Finol, E. and Amon, C. (2000) "Pulsatile Flow Hemodynamics in Abdominal Aortic Aneurysms", In: Troyani, N. and Cerrolaza, M., eds, Proceedings of the V International Congress of Numerical Methods in Engineering and Applied Sciences—CIMENICS 2000 (Sociedad Venezolana de Métodos Numéricos en IngenierÍa, Caracas, Venezuela), pp CI81–CI90.

[14] Finol, E. and Amon, C. (2000) "Momentum Transfer in Abdominal Aortic Aneurysms: The Effect of Aneurysm Size in Steady Flow Hemodynamics", In: Yao, S.C. and Jones, A., eds, Proceedings of the ASME 34th National Heat Transfer Conference-NHTC 2000 (ASME, Pittsburgh, PA), NHTC2000–12205.

[15] Guzmán, A., Moraga, N. and Amon, C. (1997) "Pulsatile Non-Newtonian Flow in a Double Aneurysm, Proceedings of the 1997", *ASME International Mechanical Engineering Congress and Exposition*, 87–88.

[16] Guzmán, A., Moraga, N., Muñoz, G. and Amon, C. (1997) "Pulsatile Non-Newtonian Flow in a Converging-Diverging Tube", *AIChE Symposium Series* **93**, 288–294.

[17] McDonald, D. (1960) Blood Flow in Arteries (Wilkins & Wilkins, Baltimore, MD).

[18] Albritton, E. (1951) Standard Values in Blood (United States Air Force, Wright Air Development Center, Akron, OH), pp 5–7.

[19] Lei, M. and Kleinstreuer, C. (1996) "The Zero-Tension Hypothesis for the Mechanism of Atherogenesis and the Wall Shear Stress Gradient (WSSG) Predictor Equation, Proceedings of the 1996", *ASME International Mechanical Engineering Congress and Exposition*, 211–212.

[20] Patera, A. (1984) "A Spectral Element Method for Fluid Dynamics: Laminar Flow in a Channel Expansion", *Journal of Computational Physics* **54**, 468–488.

[21] Amon, C. (1993) "Spectral Element—Fourier Method for Transitional Flows in Complex Geometries", *AIAA Journal* **31**, 42–48.

[22] Amon, C. (1995) "Spectral Element—Fourier Method for Unsteady Forced Convective Heat Transfer in Complex Geometry Flows", *AIAA Journal of Thermophysics and Heat Transfer* **9**, 247–253.

[23] Muraki, N. (1983) "Ultrasonic Studies of the Abdominal Aorta with Special Reference to Hemodynamic Considerations on Thrombus Formation in the Abdominal Aortic Aneurysm", *Journal of Japanese College Angiology* **23**, 401–413.